

# Fluidized-Bed CVD of Unstacked Double-Layer Templated Graphene and Its Application in Supercapacitors

Gui-Li Tian, Qiang Zhang, Meng-Qiang Zhao, and Hao-Fan Wang  
Dept. of Chemical Engineering, Tsinghua University, Beijing 100084, China

Cheng-Meng Chen  
Key Laboratory of Carbon Materials, Institute of Coal Chemistry, Chinese Academy of Sciences, Taiyuan 030001, China

Fei Wei  
Beijing Key Laboratory of Green Chemical Reaction Engineering and Technology, Tsinghua University, Beijing 100084, China

DOI 10.1002/aic.14710

Published online December 21, 2014 in Wiley Online Library (wileyonlinelibrary.com)

Graphene is inclined to stack with each other that greatly hinders the full utilization of its intrinsic extraordinary properties. Introducing protuberant spacers is a straightforward strategy to avoid the stacking of graphene nanosheets, resulting in a novel unstacked double-layer templated graphene (DTG) structure. Herein, a family of layered double hydroxides were used for the bulk chemical vapor deposition (CVD) of DTG in a fluidized-bed reactor. A high specific surface area of  $1554.2 \text{ m}^2 \text{ g}^{-1}$  and a large pore volume of  $1.70 \text{ cm}^3 \text{ g}^{-1}$  were achieved. When used as the electrode material for supercapacitors, the DTG afforded a specific capacitance of  $65.5 \text{ F g}^{-1}$  at a sweep rate of  $5.0 \text{ mV s}^{-1}$  and a capacitance retention of 77% when the sweep rate was increased to  $500 \text{ mV s}^{-1}$ . Therefore, the DTG obtained via fluidized bed CVD is a promising electrode material for supercapacitor applications. © 2014 American Institute of Chemical Engineers AIChE J, 61: 747–755, 2015

Keywords: graphene, chemical vapor deposition, supercapacitor, layered double hydroxides, fluidized bed

## Introduction

Graphene, well known for its novel structure, has attracted tremendous attention owing to its theoretically extraordinary electrical and thermal conductivity, strong mechanical property, huge surface area, and excellent chemical stability.<sup>1–3</sup> Particularly, the intrinsic superior structural features render graphene quite attractive as alternative electrode material for the renewable energy storage and conversion systems, such as supercapacitors,<sup>4</sup> lithium-ion batteries,<sup>5,6</sup> lithium–sulfur batteries,<sup>7</sup> fuel cells,<sup>8</sup> and solar cells.<sup>9</sup> However, the graphene nanosheets were inclined to stack with each other driven by the strong p-p interaction between the individual sheets, which greatly compromised the intrinsic high specific surface area (SSA) and subsequently depressed their performance.

To avoid the stacking of graphene layers, myriad approaches have been developed. The introduction of other hard species, serving as the spacers, into their interlayer space is the most straightforward strategy. The commonly used spacers are conducting polymers,<sup>10</sup> nanoparticles,<sup>11,12</sup> even carbon nanotubes,<sup>13–16</sup> and so forth. However, the intercalation of these spacers into the graphene nanosheets is always complicated and introduces many interfaces into the composites inevitably that

retard the intrinsic properties of graphene. Note that the wrinkles and curvatures of graphene can restrain their stacking to some extent. Although not sufficiently, this is the main reason that single-layer graphene can be thermally stable. Inspired by this point, a unique unstacked double-layer templated graphene (DTG) structure with numerous graphene protuberances propping up in the interlayer space as pillars was proposed recently by our research group.<sup>17</sup> The unstacked DTG was fabricated in a fixed bed reactor with the mesoporous layered double oxide (LDO) as the template. It is composed of two graphene layers separated by a large amount of mesosized protuberances and exhibits excellent high-rate performance when used as electrode material for high-power lithium–sulfur batteries. The broad applications of DTG can be further explored if DTG with controllable nanostructures can be produced in large scale.

In this contribution, bulk growth of the unstacked DTG was explored in a fluidized-bed reactor. MgAl layered double hydroxides (LDHs) were used as the catalyst precursors for mesoporous LDO template formation. The nanostructures of the as-obtained DTG were well tuned by modulating the Mg/Al mole ratio in the LDH precursors. The as-obtained DTG afforded much higher capacity than routine graphene (e.g., reduced graphene oxide) when used as the electrodes for supercapacitors.

## Experimental

### Catalyst preparation

A urea assisted coprecipitation reaction was used to prepare the MgAl-LDH catalysts. Typically,  $\text{Mg}(\text{NO}_3)_2 \cdot 6\text{H}_2\text{O}$ ,

Additional Supporting Information may be found in the online version of this article.

Correspondence concerning this article should be addressed to Q. Zhang at zhang-qiang@mails.tsinghua.edu.cn.

Al(NO<sub>3</sub>)<sub>3</sub>·9H<sub>2</sub>O, and urea were dissolved in 1000 mL deionized water with [Al<sup>3+</sup>] = 0.050 mol L<sup>-1</sup>, n(Mg):n(Al) = 2.0:1, [urea] = 3.0 mol L<sup>-1</sup>. The molar ratios of Mg to Al were controlled at 2.0, 2.5, and 3.0 for LDH-2.0, LDH-2.5, and LDH-3.0, respectively. The as-obtained solution was transferred to a 2000-mL glass flask (equipped with a reflux condenser) and was kept at 100°C under continuous magnetic stirring for 12.0 h. Following that, the suspension was maintained at 94°C for 12.0 h without stirring. MgAl LDHs were finally collected after filtering, washing, and freeze-drying of the above suspension.

The Gibbs free energy for the synthesis of MgAl LDHs (take LDH-2.0 as an example) was estimated to be -1206.1 kJ mol<sup>-1</sup> (25°C) (details can be found in Supporting Information), indicating the thermodynamical preference of this reaction. Besides, the conversions of Mg(NO<sub>3</sub>)<sub>2</sub>·6H<sub>2</sub>O and Al(NO<sub>3</sub>)<sub>3</sub>·9H<sub>2</sub>O into MgAl LDHs through the urea assisted coprecipitation were around 85.6 and 98.5%, respectively. Therefore, the synthesis of MgAl LDHs as the catalysts for graphene deposition was feasible for bulk production.

### DTG growth in a fluidized bed reactor

A high-temperature fluidized-bed chemical vapor deposition (CVD) growth was applied to produce the unstacked DTG with MgAl LDHs as the catalyst precursors. The main apparatus is a quartz fluidized bed reactor with an inner diameter of 50 mm and a height of 1200 mm. A gas distributor made of porous sintered quartz plate was located at the middle of the reactor to support the solid catalysts and products at the same time. About 10.0 g MgAl LDH powder was fed into the fluidized-bed reactor. Then, the reactor was inserted into a vertical electric tube furnace and heated to 950°C under upflowing Ar atmosphere in a flow rate of 3.75 L min<sup>-1</sup> which was sufficient to guarantee the powder to spread out. The upflowing gas entered the reactor from the bottom and then passed through the gas distributor and the fluidized bed unit, and then flowed out from the top of the reactor. When reaching the reaction temperature, the calcination was maintained for 30 min in Ar atmosphere and then the upflowing Ar gas was changed to the gas mixture of CH<sub>4</sub>/Ar with the flow rate of 2.75/0.40 L min<sup>-1</sup>. The reaction was maintained for 10 min at 950°C and then the fluidized bed reactor was cooled down to room temperature under Ar protection. The as-obtained products were the nanocomposites of DTG and MgAl LDO flakes.

The catalytic decomposition of methane was proceeding as the following formula indicated: CH<sub>4</sub> → C + 2H<sub>2</sub>. A Gibbs free energy DG<sup>h</sup> = -43.489 kJ mol<sup>-1</sup> (calculated by HSC 5.1) at 950°C was calculated.

The as-grown raw products were purified by HCl (5.0 mol L<sup>-1</sup>) aqueous solution at 80°C for 12.0 h and NaOH (15.0 mol L<sup>-1</sup>) aqueous solution at 150°C for 12.0 h sequentially, to remove the MgAl LDO flakes. After filtering, washing, and freeze-drying, the unstacked DTG was finally available. The control graphene sample of routine reduced graphene oxide G1000 was produced as follows briefly: first, graphene oxide was prepared by a modified Hummers' method; then, the graphene oxide was thermally reduced at 1000°C, a comparative temperature with that for DTG growth.

### Structural characterization

The morphology and microstructure of the LDHs and the as-grown products were observed with a JSM 7401F scan-

ning electron microscopy (SEM) operated at 3.0 kV and a JEM 2010 transmission electron microscope (TEM) operated at 120.0 kV. The high resolution TEM observation at atomic level was performed on a Titan3 60-300 (FEI Company) microscope operated at 80 kV. X-ray diffraction (XRD) patterns were recorded on a Bruker D8 Advance diffractometer equipped with a Cu-K<sub>α</sub> radiation source. The thermogravimetric analysis (TGA) was performed using a Mettler Toledo TGA/DSC-1 analyzer under O<sub>2</sub> atmosphere. The Raman spectra were obtained with He-Ne laser excited at 633 nm using Horiba Jobin Yvon LabRAM HR800 Raman Spectrometer. The pore volume, size distribution, and Brunauer-Emmett-Teller (BET) SSA of the graphene samples were calculated from the N<sub>2</sub> adsorption-desorption isotherms measured by Autosorb-IQ<sub>2</sub>-MP-C system. Before the measurement, samples were degassed at 300°C until a manifold pressure of 2.0 mm Hg was reached.

### Electrochemical measurements

A typical three-electrode system was used to carry out the electrochemical measurements. Thereinto, a Ni foam coated with active material served as the working electrode, a Pt gauze electrode and Hg/HgO electrode served as the counter and reference electrode, respectively. The measurements were performed in 6.0 mol L<sup>-1</sup> KOH aqueous electrolyte at room temperature using a computer-controlled potential station (CHI 760D, CH Instrument, Austin/Texas, USA). The working electrode was prepared by loading a mixture slurry of 90 wt % active material and 10 wt % poly(vinylidene fluoride) (dissolved in N-methylpyrrolidone) on a Ni foam (1 × 1 cm<sup>2</sup>) and dried at 60°C for 6.0 h. The coated Ni foam was then pressed at a pressure of 10.0 MPa and further dried at 80°C for overnight. The areal loading mass of active materials was 2.0-3.0 mg cm<sup>-2</sup>. The cyclic voltammetry was carried out in the potential range of -1.0 to 0.0 V vs. Hg/HgO electrode at the scanning rate varying from 5.0 to 500 mV s<sup>-1</sup>.

## Results and Discussion

### Growth of DTG on MgAl LDO flakes in a fluidized bed reactor

In this contribution, a family of MgAl LDHs with different Mg/Al molar ratios were prepared as the catalyst precursors. LDHs are a class of synthetic two-dimensional nanostructured anionic clays, in which most metals (e.g., Li, Mg, Al, Ca, Mn, Fe, Co, Ni, Cu, and Zn) can be dispersed on the atomic level in a lamellar flake with controllable components.<sup>18,19</sup> Herein, LDH-2.0 was selected as an example to demonstrate the fluidized bed CVD synthesis and the nanostructure of the as-obtained DTG. The MgAl LDHs were hexagonal flakes with an average lateral size of about 2 μm and a uniform thickness of about 10 nm (Figure 1a). They were well crystallized with intensive sharp characteristic (003), (006), and (009) peaks in the powder XRD pattern (Figure 1b). The mass production of DTG was carried out in a fluidized-bed reactor with Ar as the carrier gas and CH<sub>4</sub> as the carbon source. The LDH-based catalysts exhibited a well fluidized state under a gas velocity of about 11 cm s<sup>-1</sup> during the whole reaction process.<sup>20</sup> Before the introduction of carbon source for graphene deposition, the MgAl LDHs were first calcined at 950°C to transform into MgAl LDOs composed of MgAl<sub>2</sub>O<sub>4</sub> spinel and MgO, as indicated in the

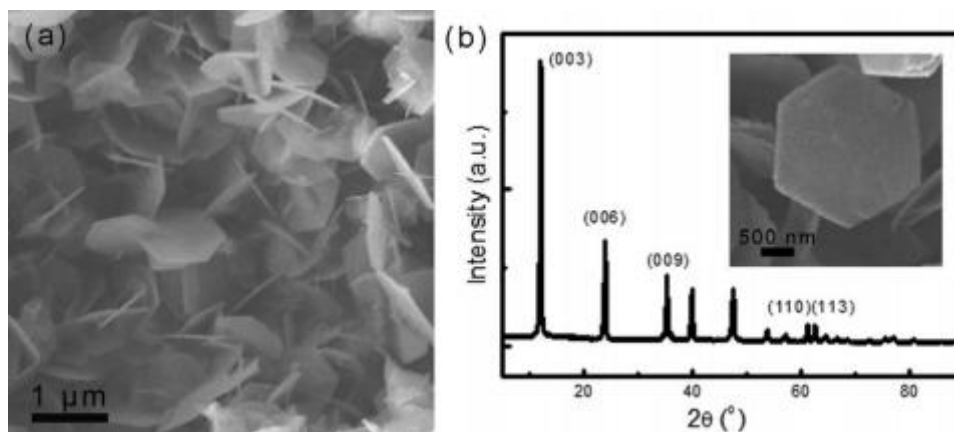


Figure 1. (a) SEM image of MgAl LDH with the Mg/Al element ratio of 2:1. (b) XRD pattern of MgAl LDH. The inset picture presents the SEM image of one LDH flake.

powder XRD pattern (Figure 2a). During the topotactic transformation from MgAl LDHs to LDOs, large quantities of Kirkendall voids were formed due to the different diffusivities of Mg and Al atoms, along with the release of H<sub>2</sub>O and CO<sub>2</sub> molecules, leading to the mesoporous structure of

LDOs.<sup>21</sup> The N<sub>2</sub> adsorption–desorption analysis (Supporting Information Figure S1) showed the pore-size distribution of MgAl LDOs, confirming the existence of numerous mesopores in the LDO flakes with a total pore volume of 0.26 cm<sup>3</sup> g<sup>-1</sup>. Note that the MgAl LDOs retained the plate-

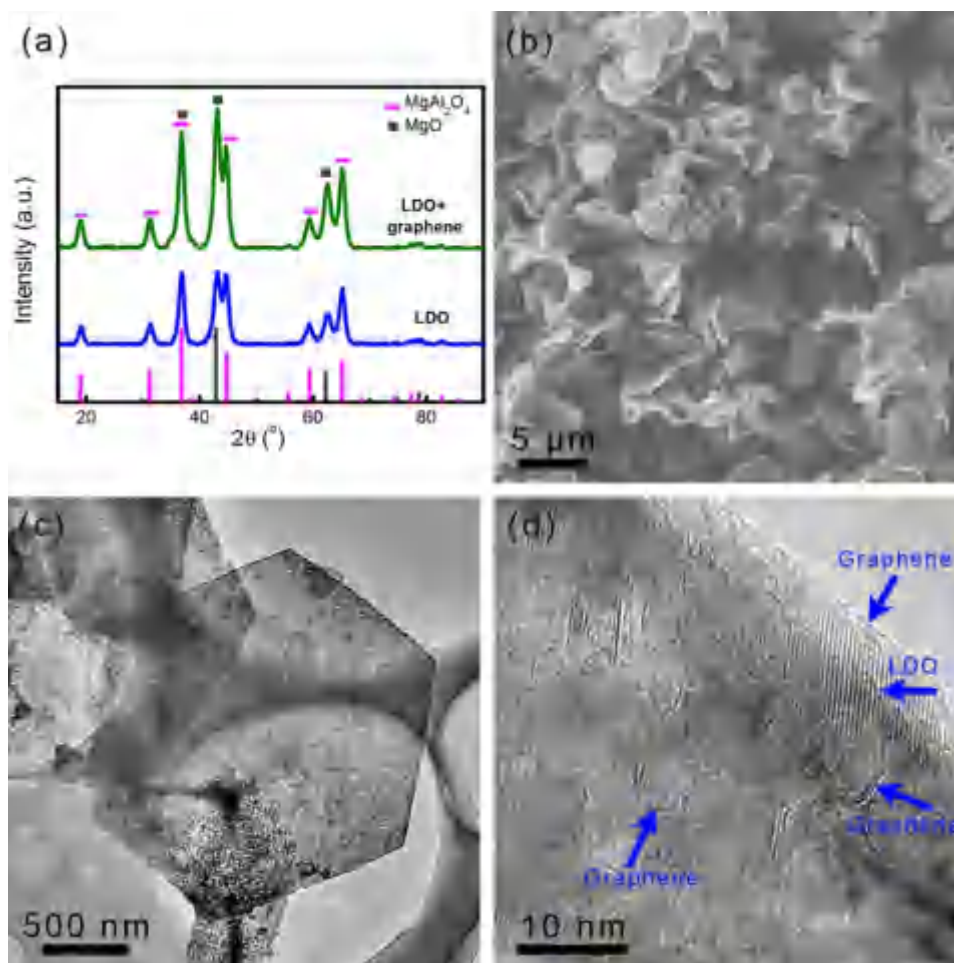


Figure 2. (a) XRD patterns of the MgAl LDOs obtained by calcination of MgAl LDHs at 950°C and the graphene/LDO nanocomposites. The pink and dark gray standard XRD patterns at the bottom correspond to MgAl<sub>2</sub>O<sub>4</sub> (PDF#21-1152) and MgO (PDF#45-0946), respectively. (b) SEM image and (c, d) TEM images of the as-produced DTG grown on the MgAl LDH catalyst. The blue arrows indicate the graphene nanosheets cast onto both the surface and inner wall of the mesopores of the LDO flake.

[Color figure can be viewed in the online issue, which is available at [wileyonlinelibrary.com](http://www.wileyonlinelibrary.com).]

like morphology even with many mesopores distributed in the flakes, which was attributed from the well oriented attachment of  $\text{MgAl}_2\text{O}_4$  spinel and  $\text{MgO}$ . Therefore, the lamellar  $\text{MgAl}$  LDO flakes with an oxygen-terminated surface and high thermal stability were good templates and catalysts for the deposition of graphene. Once introducing  $\text{CH}_4$  into the reactor at  $950^\circ\text{C}$ , the carbon source decomposed with a conversion of 7.0% at the LDO surface and carbon atoms recombined into graphene layers not only at the surface but also at the inner walls of the mesopores. The as-obtained graphene/LDO nanocomposites exhibited a very similar powder XRD pattern with that of  $\text{MgAl}$  LDOs (Figure 2a). The typical characteristic diffraction peak of graphite at  $26.4^\circ$  was indiscernible, indicating that graphene deposited on the LDO surface was almost single layer. The as-obtained graphene/LDO nanocomposites exhibited similar plate-like morphology with  $\text{MgAl}$  LDHs (Figures 2b, c). The deposited graphene layers were observed evidently at the edge and in the pores of the LDO flakes under high-resolution TEM (Figure 2d).

The LDO template can be thoroughly removed by routine purification in  $\text{HCl}$  and  $\text{NaOH}$  aqueous solution sequentially and the final DTG products were available with a yield of  $0.21 \text{ g}_{\text{DTG}}/\text{g}_{\text{cata}}$ . The SEM and TEM images in Figure 3 presented the well-preserved plate-like morphology of the purified DTG sample. Some graphene circles with a size of several nanometers were located on the as-obtained graphene layers as marked by the blue arrows in Figure 3d. These were identified as the very short graphene protuberances cast into the mesopores in the LDOs. Moreover, the atomic force microscopy (AFM) image of the DTG shown in Supporting Information Figure S2 displayed that the thickness of one DTG flake was about 10 nm. The interval distance between the double graphene layers of DTG was enlarged to several nanometers, which strongly demonstrated the unstack character of DTG. Besides, the presence of graphene protuberances was clearly recognized from the AFM image, which effectively prevent the stacking of the two graphene layers deposited on both sides of one LDO flake. Consequently, the as-fabricated DTG was with a box-like structure mainly constituted of double unstacked graphene layers outside and large quantities of graphene protuberances inside serving as the pillars. The magnified TEM image in Figure 3e showed the large-size graphene domains in one DTG piece. The as-produced DTG exhibited good thermal stability (Figure 3f). The TGA profile exhibited a sharp weight loss peak around  $600^\circ\text{C}$  and a total weight loss of almost 100%, indicating that the high purity of the purified DTG. There was about 0.9 at% oxygen on the surface of the DTG with primary  $\text{sp}^2$  hybridized carbon atoms. This is much lower than the routine reduced graphene oxide via thermal reduction (O content 2.9 at% obtained by  $1000^\circ\text{C}$  treatment)<sup>22</sup> and chemical reduction (O content of 5–10 at%),<sup>23,24</sup> This was attributed from the large graphene domain formed at a high temperature of  $950^\circ\text{C}$  growth on the metal oxide catalysts. The self-healing of defects with the assistant of metal oxide catalysts was also beneficial for large size graphene formation.<sup>17</sup>

There were a family of synthesis routes to obtain graphene, such as mechanical exfoliation,<sup>1</sup> thermal or chemical reduction of graphite oxide (GO),<sup>3,25</sup> epitaxial growth under high temperature based on silicon carbide,<sup>26</sup> and CVD of graphene on metal/metal oxide templates.<sup>27,28</sup> Among them, chemically derived graphene products from GO were widely explored. Nevertheless, due to the strong oxidation during GO prepara-

tion, both the chemical or thermal removal of oxygen groups in the GO induced high-density defects in the reduced graphene oxide nanosheets. This renders chemically derived graphene a low electrical conductivity of  $0.05\text{--}2.0 \text{ S cm}^{-1}$  but excellent active sites for pseudocapacitor, selective absorption, and excellent reactivity for oxygen reduction and selective oxidation.<sup>4,22,29–33</sup> On the contrary, graphene prepared by CVD growth usually exhibited good graphitic degree and high conductivity ( $10^1\text{--}5 \times 10^2 \text{ S cm}^{-1}$ ).<sup>17,34</sup> Herein, the as-produced DTG-2 was with a high electrical conductivity of  $368 \text{ S cm}^{-1}$ , which was attributed from the large graphene domain and three-dimensional (3D) interconnected nanostructures of DTG. The fluidized bed reactor is efficient to produce high-quality DTG. The fluidized bed has advantages of enough growth space, excellent diffusion and heat transfer, easiness in scaling up and continuous operation. Therefore, the fluidized bed CVD has been world widely accepted as large scale CVD reactor for nanocarbon production.<sup>35–39</sup>

### Structure modulation of DTG

To modulate the structure of the as-produced DTG, a family of  $\text{MgAl}$  LDHs with different  $\text{Mg/Al}$  molar ratios were used as the catalyst precursors. With the  $\text{Mg/Al}$  ratio ranging from 2.0 to 3.0, all the  $\text{MgAl}$  LDOs preserved their plate-like structure (see in Figures 4a, b) after high-temperature calcination. When using LDH-2.5 and LDH-3.0 as the catalyst precursors, the corresponding DTG products (denoted as DTG-2.5 and DTG-3.0, respectively) (Figure 4) exhibited resembling morphology with the DTG-2.0 and the graphene yield was slightly increased (0.24 and 0.31  $\text{g}_{\text{DTG}}/\text{g}_{\text{cata}}$  for DTG-2.5 and DTG-3.0, respectively). There were also thin graphene layers at the edge and graphene circles on the DTG products, which were clearly indicated by the blue arrows in the TEM images of Figures 4c, d. Similarly, high-resolution TEM images (Figures 4e, f) indicated that the purified DTG products were with many graphene protuberances propping up the double graphene layers. Hence, due to the contribution of the graphene protuberance pillars, the interlayer space between the unstacked graphene layers was swelled and the as-obtained DTG materials were porous. Particularly, the SSA of the DTG-2.0, DTG-2.5, and DTG-3.0, calculated by the multipoint BET method from the  $\text{N}_2$  adsorption/desorption isotherms (see in Figure 5a), was 1554.2, 1422.1, and 1481.4  $\text{m}^2 \text{ g}^{-1}$ , respectively. The pore-size distribution for these three DTG samples was presented in Figure 5b, demonstrating the existence of abundant mesopores. The corresponding total pore volumes were 1.70, 1.32, and 1.27  $\text{cm}^3 \text{ g}^{-1}$  in turn. Considering the simultaneous deposition of graphene both at the surface and the wall of open pores in LDO flakes, the roots of the graphene protuberances were covalently bonded with the graphene layers. As a result, there were pentagonal and heptagonal carbon rings at the covalent-bonding connections between the graphene protuberances and graphene sheets. Accordingly, strong D bands can be detected in the Raman spectra (Figures 5c–e). The Raman spectra were deconvoluted into five bands for spectral analysis, which were a combination of four Lorentzian-shaped bands (D1, D2, D4, and G) at approximately 1330, 1620, 1200, and 1580  $\text{cm}^{-1}$ , respectively, with a Gaussian-shaped band D3 at approximately 1500  $\text{cm}^{-1}$ . Generally, G band was assigned to the vibration mode of ideal graphitic lattice ( $E_{2g}$ -symmetry) and the D bands were ascribed to the vibration modes of disordered

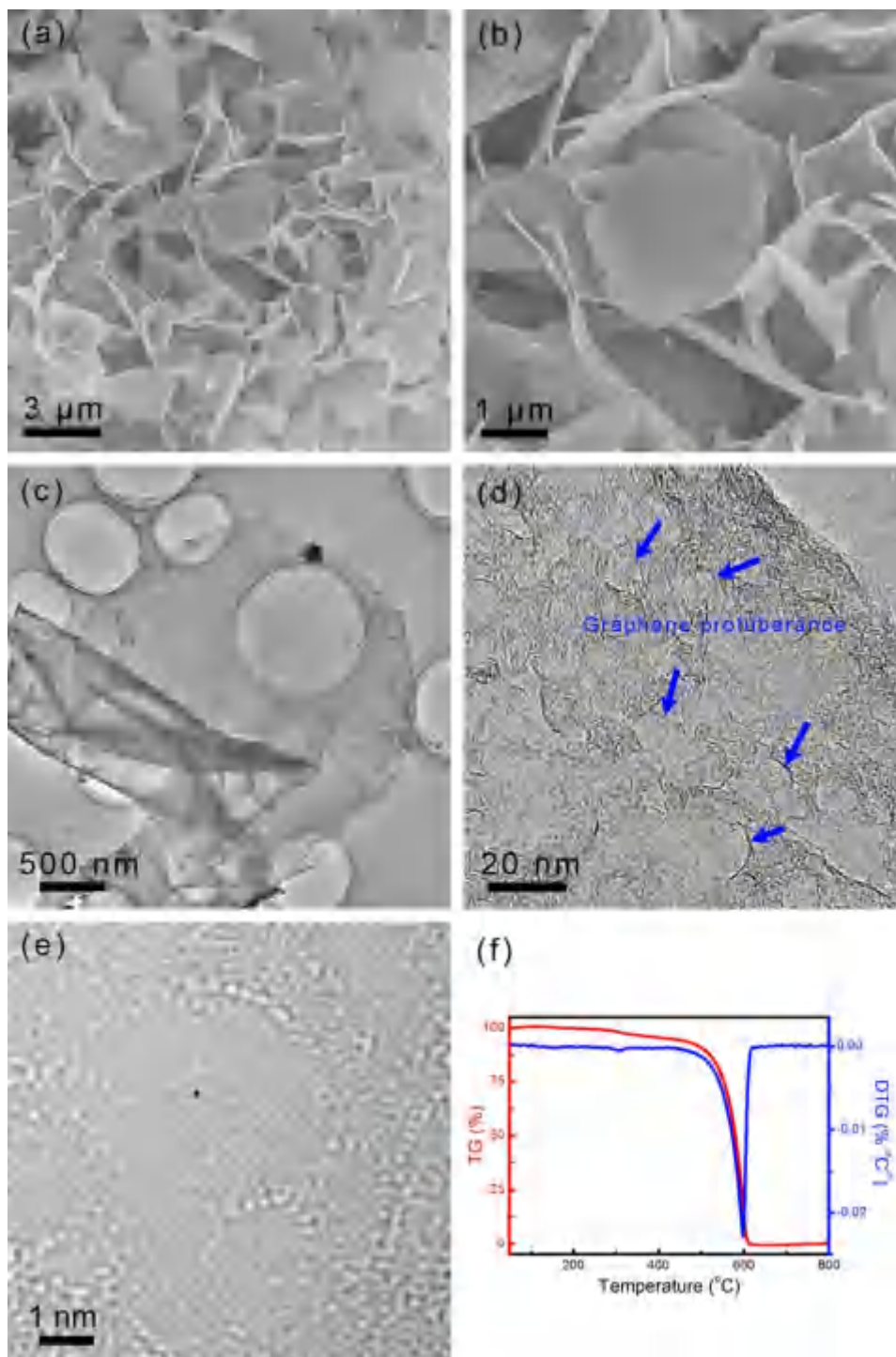


Figure 3. (a, b) SEM, (c, d) TEM, and (e) high resolution TEM images of the purified DTG. The distinct graphene protuberances are highlighted by the blue arrows. (f) The TGA profiles of the as-obtained DTG in O<sub>2</sub> atmosphere.

[Color figure can be viewed in the online issue, which is available at [wileyonlinelibrary.com](http://wileyonlinelibrary.com).]

graphitic lattice and amorphous carbon, among which D1 band was widely adapted as the “defect” band.<sup>40</sup> All the band parameters for the curve fitting were summarized in Supporting Information Table S1. Notably, with the Mg/Al ratio in the LDH precursor decreasing from 3.0 to 2.5 to 2.0, the peak area ratio (D1/G) gradually increased from 2.90 to 3.06 to 3.49. This can be explained by the fact that with a lower Mg/Al ratio, there were more Mg-Al diffusion couples during the calcination. Hence, the Kirkendall diffusion was enhanced, and subsequently more mesopores were obtained

in the LDO flakes. In this respect, more graphene protuberances were grown, which induced more defects in the final DTG. In fact, the density of the graphene protuberances in the DTG samples were statistically counted as 5.3, 6.5, and  $7.3 \times 10^{14} \text{ m}^{-2}$ , respectively, with the Mg/Al ratio decreasing from 3.0 to 2.5 to 2.0 (Table 1). The protuberance size was mainly in the range of 2–12 nm (Figure 5b and Supporting Information Figure S3). As a result of more protuberance pillars, DTG-2.0 afforded larger SSA and higher porosity than the other two DTG samples.

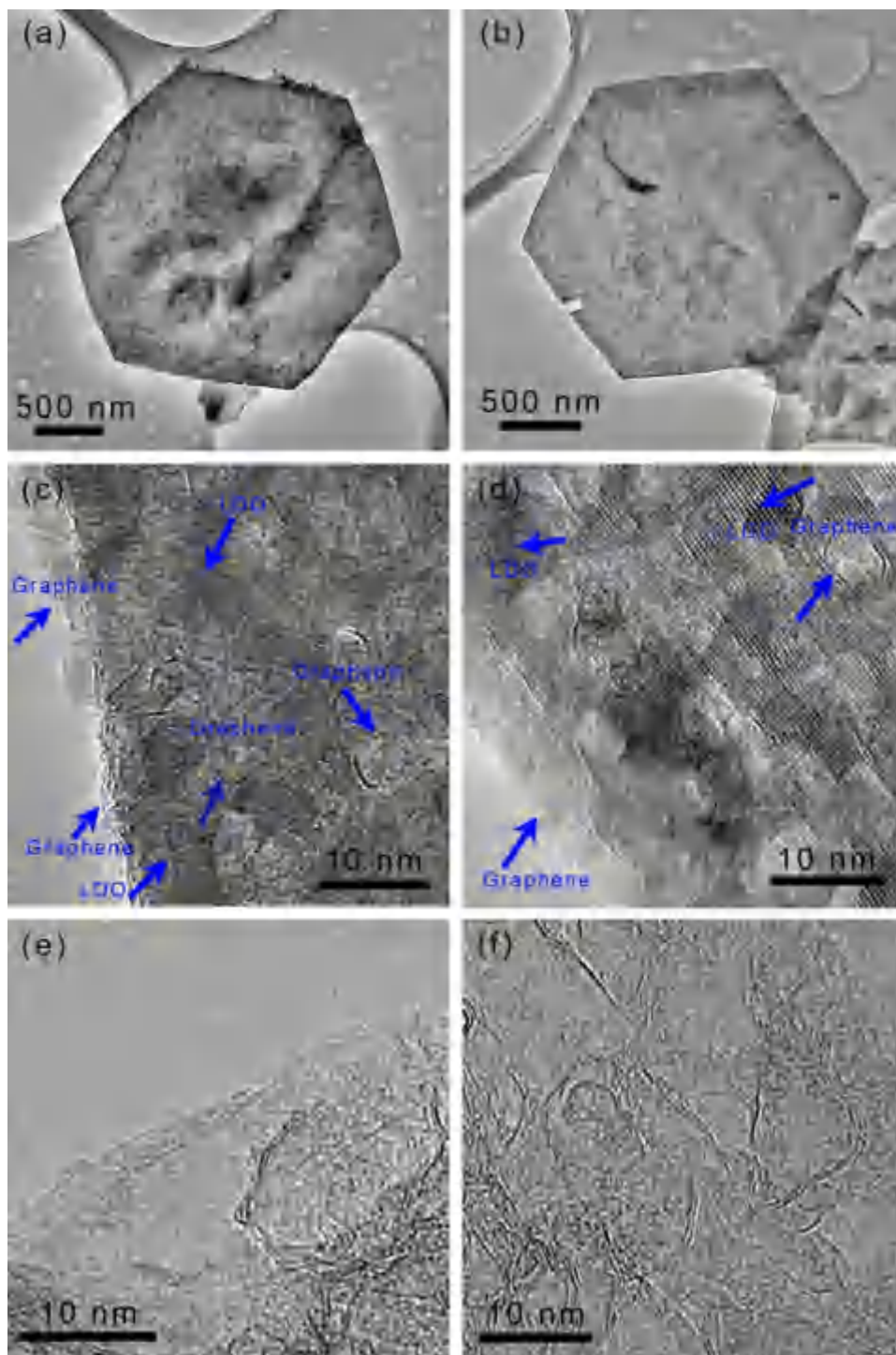


Figure 4. TEM images of the as-obtained DTG products with the catalyst of (a, c, e) LDH-2.5 and (b, d, f) LDH-3.0, respectively. (a-d) indicate the raw graphene/LDO nanocomposites while (e) and (f) are for the corresponding purified DTG samples.

[Color figure can be viewed in the online issue, which is available at [wileyonlinelibrary.com](http://wileyonlinelibrary.com).]

#### DTG electrode for supercapacitors

Together with the high conductivity, large SSA, and excellent porosity derived from the protuberance pillared graphene, the DTG was expected to be promising electrode material for electrochemical energy storage. Capacitive performance was selected as the probe to evaluate the electrochemical properties of DTG. This was performed in a three-electrode cell with  $6.0 \text{ mol L}^{-1}$  KOH aqueous solution as

the electrolyte. In addition, a routine chemical-derived graphene G1000 sample produced via thermal reduction of graphene oxide was applied as a control sample for the capacitance characterization. The G1000 was with a SSA of  $434.1 \text{ m}^2 \text{ g}^{-1}$ , a pore volume of  $3.14 \text{ cm}^3 \text{ g}^{-1}$ , and an oxygen content of 2.9 at%.<sup>22</sup> The GO-derived G1000 exhibited more graphitic defects than the DTG samples. As shown in Supporting Information Figure S4 and Table S1, the peak

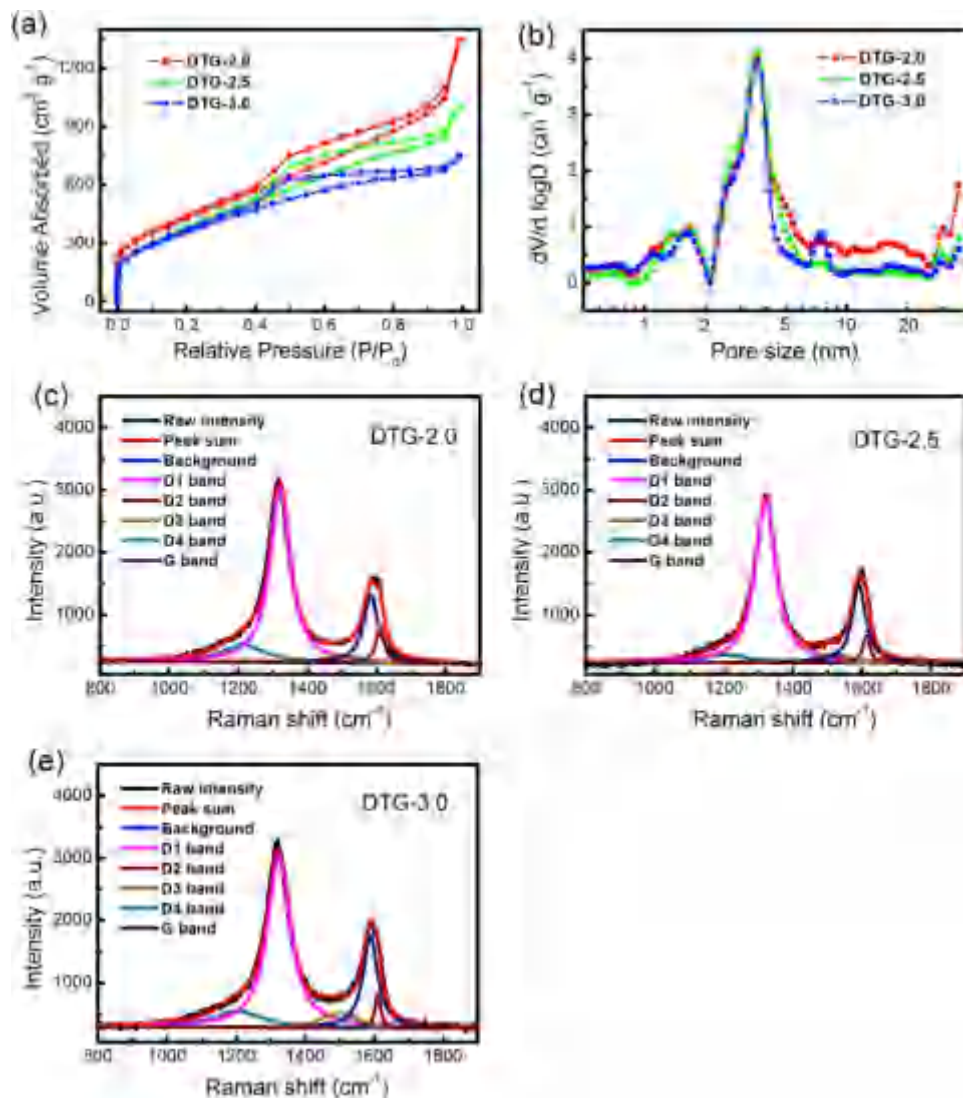


Figure 5. (a)  $N_2$  adsorption-desorption isotherms, (b) pore-size distribution, and (c, d, e) curve fitting for Raman spectra of the DTG products grown on LDH-2.0, LDH-2.5, and LDH-3.0 catalyst, respectively.

[Color figure can be viewed in the online issue, which is available at [wileyonlinelibrary.com](http://wileyonlinelibrary.com).]

area ratios of D bands (D1, D3, and D4) to G band for G1000 were all higher than that for DTG samples. The D2 band was assigned to a lattice vibration of the surface graphene layers which was in an analogous mode to that of the G band ( $E_{2g}$ -symmetry).<sup>40</sup> Considering the contribution of many graphene protuberances, the DTG products possessed more graphene layers at the surface than G1000, leading to rational higher D2/G ratio.

CV measurements were first carried out at different potential sweep rates varying from 5.0 to 500  $mV s^{-1}$ . As indicated in Figures 6a, b, the CV profiles for both G1000 and DTG maintained nearly ideal rectangular shape in a broad range of the potential sweep rates, implying that the total capacitance

Table 1. A Summary of the Nanostructures of the DTG Products

Sample	Catalyst	SSA ( $m^2 g^{-1}$ )	Pore Volume ( $cm^3 g^{-1}$ )	Areal Density of Protuberance ( $m^{-2}$ )
DTG-2.0	LDH-2.0	1554.2	1.70	$7.3 \times 10^{14}$
DTG-2.5	LDH-2.5	1422.1	1.32	$6.5 \times 10^{14}$
DTG-3.0	LDH-3.0	1481.4	1.27	$5.3 \times 10^{14}$

was predominantly attributed from the electric double-layer capacitance. It was in accordance with the fact that the as-obtained graphene via the CVD growth or post-treatment at high temperature contained few oxygen-containing functional groups and accordingly little pseudocapacitance contributed to the total capacitance. However, the DTG electrode presented much larger area enclosed by the CV curve at the same potential sweep rate, indicating a higher capacitance of the DTG than that of the G1000. To compare the rapid charge/discharge abilities of the graphene, the specific capacitances at different potential sweep rates were calculated from the corresponding CV curves and displayed in Figure 6c. With the sweep rate increasing from 5.0 to 500  $mV s^{-1}$ , the specific capacitance of the DTG electrode was slightly decreased from 65.5 to 50.3  $F g^{-1}$ , that is, about 77% of the initial capacitance was preserved. In contrast, the initial capacitance of the G1000 electrode was 53.2  $F g^{-1}$  at a sweep rate of 5.0  $mV s^{-1}$ . However, only approximately 62% capacitance was preserved when the sweep rate increased to 500  $mV s^{-1}$ . Hence, DTG exhibited larger capacitance and superior rapid charge/discharge properties than G1000. In contrast with the reduced graphene oxide with large amounts of oxygen containing

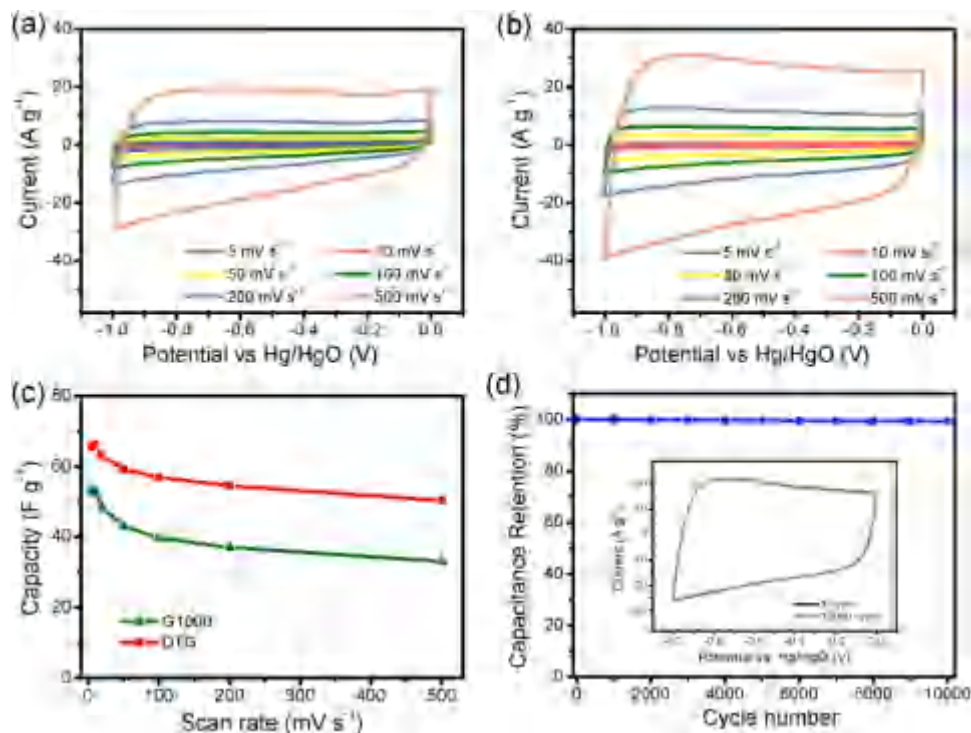


Figure 6. Cyclic voltammograms of (a) G1000 and (b) DTG with the sweep rates from 5.0 to 500  $\text{mV s}^{-1}$ . (c) The specific capacitance versus sweep rates for G1000 and DTG. (d) Cycling performance of DTG electrode. Inset shows the CV profiles of the 1st and 10,000th cycle at a scan rate of 400  $\text{mV s}^{-1}$  in 6.0  $\text{mol L}^{-1}$  KOH electrolyte.

[Color figure can be viewed in the online issue, which is available at [wileyonlinelibrary.com](http://wileyonlinelibrary.com).]

functional groups,<sup>22,41,42</sup> the contribution of pseudocapacitance contributed by the redox reaction on functional groups can be neglected. Herein, the electrical double-layer capacitance of DTG electrode was main contribution, which was much improved compared with other heteroatom-free carbon materials.<sup>43–46</sup> There were a large quantity of graphene protuberances between the DTG, the swelled interspace supplied extra accessible surface area and effective transport channels that facilitated the rapid transfer of massive ions to build the electrical double layer capacitor. In the case of G1000, there were no protuberance pillars and the graphene nanosheets were stacked with each other due to the strong van der Waals force. Therefore, the theoretical specific area of graphene, as well as the ion transfer channels, was much restricted resulting in the depressed electrical supercapacitor performance.

In addition, the durability of the DTG material was also evaluated in a three-electrode electrochemical cell by repeating CV charge/discharge process at a scan rate of 400  $\text{mV s}^{-1}$ . The capacitance retention of DTG as a function of cycle number with a potential window of  $-1.0$  to  $0$  V vs. Hg/HgO was shown in Figure 6d. After 10,000 times of cycling, the DTG electrode still held 99.2% of the initial capacitance, illustrating a very good cycling stability. Consequently, the DTG was demonstrated to be a promising electrode material for supercapacitors with excellent durability.

## Conclusions

The unstacked DTG was bulk grown in a fluidized bed reactor through facile CVD on metal-oxide catalysts. With the LDH-derived mesoporous MgAl LDO flakes as the template and catalyst, graphene deposited both at the surface and the inside walls of the mesopores of the LDO flakes. As a result,

the as-fabricated DTG exhibited a 3D box-like structure with large quantities of graphene protuberances propping up the double graphene layers, leading to its novel features of large SSA (as high as  $1554.2 \text{ m}^2 \text{ g}^{-1}$ ) and abundant porosity (up to  $1.70 \text{ cm}^3 \text{ g}^{-1}$ ). By adjusting the Mg/Al ratios in the LDH precursors, the SSA, porosity, and defect density of the DTG products can be well tuned. Such unique structural features endow the DTG with good capacitive performance. The DTG electrode offered a specific capacitance of  $65.5 \text{ F g}^{-1}$ , much higher than the routine reduced graphene oxide via post thermal reduction under high temperature at a sweep rate of 5.0  $\text{mV s}^{-1}$ . Besides, good retention capability, that is, 77% capacitive retention was preserved when the sweep rate was increased to 500  $\text{mV s}^{-1}$ , was achieved. These were ascribed to the effective micro/mesoporous 3D conductive carbon scaffold granting fast charge transfer. Therefore, the unstacking character stemming from the graphene protuberances propping up between the double graphene layers rendered DTG with intrinsic large SSA, abundant tunable micro/mesopores, and 3D conductive scaffolds, which result in an attractive electrode for energy conversion and storage via supercapacitors, Li-ion batteries, and Li-S batteries. Besides, the unique structured DTG synthesized through high-temperature CVD was expected to possess remarkable thermal and electrical conductivity. Combined with further exploration on modulating the surface chemistry and bulk material construction, we foresee promising bulk applications of DTG for advanced energy storage, nanocomposites, heterogeneous catalysis, as well as controllable drug delivery.

## Acknowledgment

This work was supported by the Natural Scientific Foundation of China (No. 21422604).

## Literature Cited

- Novoselov KS, Geim AK, Morozov SV, Jiang D, Zhang Y, Dubonos SV, Grigorieva IV, Firsov AA. Electric field effect in atomically thin carbon films. *Science*. 2004;306:666–669.
- Geim AK. Graphene: Status and prospects. *Science*. 2009;324:1530–1534.
- Zhu YW, Murali S, Cai WW, Li XS, Suk JW, Potts JR, Ruoff RS. Graphene and graphene oxide: synthesis, properties, and applications. *Adv Mater*. 2010;22:3906–3924.
- Huang Y, Liang JJ, Chen YS. An overview of the applications of graphene-based materials in supercapacitors. *Small*. 2012;8:1805–1834.
- Sun YQ, Wu QO, Shi GQ. Graphene based new energy materials. *Energy Environ Sci*. 2011;4:1113–1132.
- Luo B, Liu SM, Zhi LJ. Chemical approaches toward graphene-based nanomaterials and their applications in energy-related areas. *Small*. 2012;8:630–646.
- Wang DW, Zeng QC, Zhou GM, Yin LC, Li F, Cheng HM, Gentle IR, Lu GQ. Carbon-sulfur composites for Li-S batteries: status and prospects. *J Mater Chem A*. 2013;1:9382–9394.
- Qu LT, Liu Y, Baek JB, Dai LM. Nitrogen-doped graphene as efficient metal-free electrocatalyst for oxygen reduction in fuel cells. *ACS Nano*. 2010;4:1321–1326.
- Chen D, Zhang H, Liu Y, Li JH. Graphene and its derivatives for the development of solar cells, photoelectrochemical, and photocatalytic applications. *Energy Environ Sci*. 2013;6:1362–1387.
- Zhang K, Zhang LL, Zhao XS, Wu JS. Graphene/polyaniline nanoribbon composites as supercapacitor electrodes. *Chem Mater*. 2010;22:1392–1401.
- Wu ZS, Zhou GM, Yin LC, Ren W, Li F, Cheng HM. Graphene/metal oxide composite electrode materials for energy storage. *Nano Energy*. 2012;1:107–131.
- Yan J, Wei T, Shao B, Ma FQ, Fan ZJ, Zhang ML, Zheng C, Shang YC, Qian WZ, Wei F. Electrochemical properties of graphene nanosheet/carbon black composites as electrodes for supercapacitors. *Carbon*. 2010;48:1731–1737.
- Tian GL, Zhao MQ, Yu DS, Kong XY, Huang JQ, Zhang Q, Wei F. Nitrogen-doped graphene/carbon nanotube hybrids: in situ formation on bifunctional catalysts and their superior electrocatalytic activity for oxygen evolution/reduction reaction. *Small*. 2014;10:2251–2259.
- Fan ZJ, Yan J, Zhi LJ, Zhang Q, Wei T, Feng J, Zhang ML, Qian WZ, Wei F. A three-dimensional carbon nanotube/graphene sandwich and its application as electrode in supercapacitors. *Adv Mater*. 2010;22:3723–3728.
- Zhao MQ, Liu XF, Zhang Q, Tian GL, Huang JQ, Zhu WC, Wei F. Graphene/single-walled carbon nanotube hybrids: one-step catalytic growth and applications for high-rate Li-S batteries. *ACS Nano*. 2012;6:10759–10769.
- Byon HR, Lee SW, Chen S, Hammond PT, Shao-Horn Y. Thin films of carbon nanotubes and chemically reduced graphenes for electrochemical micro-capacitors. *Carbon*. 2011;49:457–467.
- Zhao MQ, Zhang Q, Huang JQ, Tian GL, Nie JQ, Peng HJ, Wei F. Unstacked double-layer templated graphene for high-rate lithium-sulphur batteries. *Nat Commun*. 2014;5:3410.
- Li CM, Wei M, Evans DG, Duan X. Layered double hydroxide-based nanomaterials as highly efficient catalysts and adsorbents. *Small*. 2014;10:4469–4486.
- Fan GL, Li F, Evans DG, Duan X. Catalytic applications of layered double hydroxides: recent advances and perspectives. *Chem Soc Rev*. 2014;43:7040–7066.
- Zhao MQ, Zhang Q, Huang JQ, Nie JQ, Wei F. Layered double hydroxides as catalysts for the efficient growth of high quality single-walled carbon nanotubes in a fluidized bed reactor. *Carbon*. 2010;48:3260–3270.
- Tian GL, Zhao MQ, Zhang BS, Zhang Q, Zhang W, Huang JQ, Chen TC, Qian WZ, Su DS, Wei F. Monodisperse embedded nanoparticles derived from an atomic metal-dispersed precursor of layered double hydroxide for architected carbon nanotube formation. *J Mater Chem A*. 2014;2:1686–1696.
- Chen CM, Zhang Q, Yang MG, Huang CH, Yang YG, Wang MZ. Structural evolution during annealing of thermally reduced graphene nanosheets for application in supercapacitors. *Carbon*. 2012;50:3572–3584.
- Stankovich S, Dikin DA, Piner RD, Kohlhaas KA, Kleinhammes A, Jia Y, Wu Y, Nguyen ST, Ruoff RS. Synthesis of graphene-based nanosheets via chemical reduction of exfoliated graphite oxide. *Carbon*. 2007;45:1558–1565.
- Pei SF, Cheng HM. The reduction of graphene oxide. *Carbon*. 2012;50:3210–3228.
- He DF, Shen LM, Zhang XY, Wang YF, Bao NZ, Kung HH. An efficient and eco-friendly solution-chemical route for preparation of ultrastable reduced graphene oxide suspensions. *AIChE J*. 2014;60:2757–2764.
- Emtsev KV, Bostwick A, Horn K, Jobst J, Kellogg GL, Ley L, McChesney JL, Ohta T, Reshanov SA, Rohrl J, Rotenberg E, Schmid AK, Waldmann D, Weber HB, Seyller T. Towards wafer-size graphene layers by atmospheric pressure graphitization of silicon carbide. *Nat Mater*. 2009;8:203–207.
- Sutter PW, Flege JI, Sutter EA. Epitaxial graphene on ruthenium. *Nat Mater*. 2008;7:406–411.
- Li XS, Cai WW, An JH, Kim S, Nah J, Yang DX, Piner R, Velamakanni A, Jung I, Tutuc E, Banerjee SK, Colombo L, Ruoff RS. Large-area synthesis of high-quality and uniform graphene films on copper foils. *Science*. 2009;324:1312–1314.
- Wang LF, Yang RT, Sun CL. Graphene and other carbon sorbents for selective adsorption of thiophene from liquid fuel. *AIChE J*. 2013;59:29–32.
- Huang X, Yin ZY, Wu SX, Qi XY, He QY, Zhang QC, Yan QY, Boey F, Zhang H. Graphene-based materials: synthesis, characterization, properties, and applications. *Small*. 2011;7:1876–1902.
- Kuila T, Mishra AK, Khanra P, Kim NH, Lee JH. Recent advances in the efficient reduction of graphene oxide and its application as energy storage electrode materials. *Nanoscale*. 2013;5:52–71.
- Maiti UN, Lee WJ, Lee JM, Oh Y, Kim JY, Kim JE, Shim J, Han TH, Kim SO. 25th anniversary article: chemically modified/doped carbon nanotubes & graphene for optimized nanostructures & nanodevices. *Adv Mater*. 2014;26:40–67.
- Wang DW, Su DS. Heterogeneous nanocarbon materials for oxygen reduction reaction. *Energy Environ Sci*. 2014;7:576–591.
- Wei DC, Wu B, Guo YL, Yu G, Liu YQ. Controllable chemical vapor deposition growth of few layer graphene for electronic devices. *Acc Chem Res*. 2013;46:106–115.
- Zhang Q, Huang JQ, Qian WZ, Zhang YY, Wei F. The road for nanomaterials industry: a review of carbon nanotube production, post-treatment, and bulk applications for composites and energy storage. *Small*. 2013;9:1237–1265.
- Mleczko L, Lolli G. Carbon nanotubes: an example of multiscale developmental mechanistic view from the subnanometer to the meter scale. *Angew Chem Int Ed*. 2013;52:9372–9387.
- MacKenzie KJ, Dunens OM, Harris AT. An updated review of synthesis parameters and growth mechanisms for carbon nanotubes in fluidized beds. *Ind Eng Chem Res*. 2010;49:5323–5338.
- Philippe R, Serp P, Kalck P, Kihn Y, Bordere S, Plee D, Gaillard P, Bernard D, Caussat B. Kinetic study of carbon nanotubes synthesis by fluidized bed chemical vapor deposition. *AIChE J*. 2009;55:450–464.
- Zhang Q, Huang JQ, Zhao MQ, Qian WZ, Wei F. Carbon nanotube mass production: principles and processes. *ChemSusChem*. 2011;4:864–889.
- Sadezky A, Muckenhuber H, Grothe H, Niessner R, Poschl U. Raman micro spectroscopy of soot and related carbonaceous materials: spectral analysis and structural information. *Carbon*. 2005;43:1731–1742.
- Zhang C, Lv W, Xie XY, Tang DM, Liu C, Yang QH. Towards low temperature thermal exfoliation of graphite oxide for graphene production. *Carbon*. 2013;62:11–24.
- Tateishi H, Koinuma M, Miyamoto S, Kamei Y, Hatakeyama K, Ogata C, Taniguchi T, Funatsu A, Matsumoto Y. Effect of the electrochemical oxidation/reduction cycle on the electrochemical capacitance of graphite oxide. *Carbon*. 2014;76:40–45.
- Dreyer DR, Murali S, Zhu YW, Ruoff RS, Bielawski CW. Reduction of graphite oxide using alcohols. *J Mater Chem*. 2011;21:3443–3447.
- Zhao MQ, Zhang Q, Huang JQ, Tian GL, Chen TC, Qian WZ, Wei F. Towards high purity graphene/single-walled carbon nanotube hybrids with improved electrochemical capacitive performance. *Carbon*. 2013;54:403–411.
- Yan J, Wang Q, Wei T, Fan ZJ. Recent advances in design and fabrication of electrochemical supercapacitors with high energy densities. *Adv Energy Mater*. 2014;4:1300816.
- Frackowiak E, Beguin F. Carbon materials for the electrochemical storage of energy in capacitors. *Carbon*. 2001;39:937–950.

Manuscript received Sep. 14, 2014, and revision received Nov. 20, 2014.